

# **JGR Space Physics**

### RESEARCH ARTICLE

10.1029/2021JA029930

#### **Key Points:**

- Quasilinear model of whistler instability excited by the loss-cone electron distribution is formulated
- The theoretical result compares reasonably well against Juno observation
- This shows that the quasilinear theory is a useful tool for interpreting Jovian plasma wave emissions and radiations

### Correspondence to:

P. H. Yoon, yoonp@umd.edu

#### Citation:

Yoon, P. H., Menietti, J. D., Kurth, W. S., Allegrini, F., & Bolton, S. J. (2021). Quasilinear model of Jovian whistler mode emission. *Journal of Geophysical Research: Space Physics*, 126, e2021JA029930. https://doi.org/10.1029/2021JA029930

Received 30 AUG 2021 Accepted 11 NOV 2021

### **Author Contributions:**

Conceptualization: J. D. Menietti, S. J. Bolton
Data curation: J. D. Menietti, W. S. Kurth, F. Allegrini, S. J. Bolton
Formal analysis: J. D. Menietti, W. S. Kurth, F. Allegrini
Funding acquisition: J. D. Menietti, W. S. Kurth, F. Allegrini, S. J. Bolton
Investigation: J. D. Menietti, W. S. Kurth, F. Allegrini, S. J. Bolton
Methodology: J. D. Menietti, W. S. Kurth, F. Allegrini, S. J. Bolton
Project Administration: S. J. Bolton

**Software:** J. D. Menietti, W. S. Kurth, F. Allegrini, S. J. Bolton

Resources: J. D. Menietti, F. Allegrini,

S. I. Bolton

Validation: J. D. Menietti, W. S. Kurth, F. Allegrini, S. J. Bolton

Visualization: J. D. Menietti, W. S. Kurth, S. J. Bolton

Writing – review & editing: J. D. Menietti, W. S. Kurth, F. Allegrini

© 2021. American Geophysical Union. All Rights Reserved.

### **Quasilinear Model of Jovian Whistler Mode Emission**

P. H. Yoon<sup>1,2</sup>, J. D. Menietti<sup>3</sup>, W. S. Kurth<sup>3</sup>, F. Allegrini<sup>4,5</sup>, and S. J. Bolton<sup>4</sup>

<sup>1</sup>Institute for Physical Science and Technology, University of Maryland, College Park, MD, USA, <sup>2</sup>School of Space Research, Kyung Hee University, Yongin, Korea, <sup>3</sup>Department of Physics and Astronomy, University of Iowa, Iowa City, IA, USA, <sup>4</sup>Southwest Research Institute, San Antonio, TX, USA, <sup>5</sup>Physics and Astronomy Department, University of Texas at San Antonio, San Antonio, TX, USA

**Abstract** The whistler mode chorus emissions are pervasively detected by the Juno satellite in Jupiter's magnetospheric environment. This article pays particular attention to a sample observation made by the Juno on 3 November 2019, where typical whistler mode chorus waves are measured. The emission is characterized by a broad range of wave frequencies from below  $f_{ce}/2$ , where  $f_{ce}$  denotes the local electron cyclotron frequency, down to the lower-hybrid frequency, with a gradually downshifting frequency over time. The excitation appears to coincide with the detection of a "butterfly" pitch-angle distribution and the expected loss-cone feature associated with the energetic electrons. These anisotropic features, especially the butterfly pitch-angle distribution, gradually disappear as the waves are excited and the electron phase space distribution becomes isotropic. The aim of this article is to model the characteristics by means of quasilinear kinetic theory of the whistler instability driven by a loss-cone electron distribution function with a narrow loss-cone angle, which is to be expected from low-latitude regions of the Jovian magnetosphere. It is shown that the theoretically constructed dynamic wave spectrum is consistent with the observation made on 3 November 2019. The present finding demonstrates that the quasilinear theory can be a powerful theoretical tool for interpreting various Jovian plasma wave emissions, which includes the whistler waves, but also other wave modes.

**Plain Language Summary** NASA's Juno space probe orbiting the planet Jupiter since 2016, has detected the whistler waves. It is the same type of very low frequency electromagnetic waves generated by lightning in the Earth's atmosphere, which can be converted to whistling audio wave using a suitable receiver. This article puts forth a plasma physics based explanation of the Juno whistler wave observation. According to this theory, the spiraling motion of energetic electrons trapped in Jupiter's magnetic dipole field collectively amplify the very low frequency electromagnetic noise-like signals in a manner analogous to the process taking place in the Earth's upper atmosphere.

### 1. Introduction

The whistler mode chorus waves are important for their role in the electron energization and loss process in the Earth's radiation belt environment (Baker et al., 2013; Reeves et al., 2013; Shprits et al., 2015; Tyler et al., 2019). Similar processes may occur in the Jovian magnetospheric environment as well (Horne et al., 2008; Katoh et al., 2011; Shprits et al., 2012; Woodfield et al., 2014). Unlike the Earth, however, Jupiter's rapid rotation may lead to a different type of electron beam acceleration in the polar region, which could excite whistler instability (Allegrini et al., 2017, 2020; Elliott et al., 2018), a mechanism identified for the first time thanks to NASA's Juno mission, which has been sampling data in the Jupiter's polar region since 2016 (Kurth et al., 2018; Li et al., 2020; Mauk et al., 2018). In contrast to these, Menietti et al. (2020) surveyed the whistler-mode wave emissions in the low latitude region < 30°. As shown in the overview by Menietti et al. (2020) the whistler mode waves are pervasively observed in the Jovian magnetosphere with peak intensity near M-shells of 8–10. Jupiter is a rich source of waves other than the whistler mode waves, see, for example, Imai et al. (2017a, 2017b, 2017c) and Kurth et al. (2017), but herewith we pay attention to the whistler mode chorus emission.

Compared to Earth, the scale of the equatorial whistler-mode chorus source region at Jupiter is vastly larger, with much longer field lines connecting the equatorial to polar regions, thus the propagation time for waves with small wave normal angles to interact with electrons is much longer. The chorus source region extends from about 7 < M-shell < 12, thus bordered by the Io torus on the inner edge, and by the Europa/Ganymede torus on the outer edge (Menietti et al., 2020). There is no obvious plasmasphere at Jupiter for whistler mode chorus to refract/scatter upon entering and possibly becoming hiss (Bortnik et al., 2007, 2008; Santolík et al., 2006).

YOON ET AL.



In fact hiss emission at Jupiter appears to be very bursty compared to terrestrial hiss (Li et al., 2020; Menietti et al., 2020).

As noted by Menietti et al. (2020), near the polar region of the Jovian magnetospheric environment the free energy for the whistler mode waves is associated with field-aligned electron beam (Allegrini et al., 2017, 2020; Elliott et al., 2020), and the typical ratio of plasma-to-electron gyro-frequency,  $f_{\rm pe}/f_{\rm ce}$ , can be low, where  $f_{\rm pe} = \omega_{\rm pe}/(2\pi)$  and  $f_{\rm ce} = \Omega_{\rm e}/(2\pi)$  are plasma frequency and electron gyro-frequency, respectively. Here,  $\omega_{\rm pe} = (4\pi n_0 e^2/m_e)^{1/2}$  and  $\Omega_{\rm e} = eB_0/(m_e c)$  are the angular plasma frequency and electron cyclotron frequency, respectively,  $e, m_e, c, n_0$ , and  $B_0$  being the unit electric charge, electron mass, speed of light in vacuum, ambient density, and the ambient magnetic field intensity, in that order. In contrast, for low latitude region,  $f_{\rm pe}/f_{\rm ce}$  can be substantially higher,  $f_{\rm pe}/f_{\rm ce} > 1$ , within the Io torus. For the low-latitude region, several free energy sources can be entertained, although with a limited direct measurement of electron distribution function, it is not so easy to fully characterize the free energy source. In spite of this, we may entertain a number of possible sources for whistler wave excitation.

Among the possible mechanisms for Jovian whistler waves in the equatorial region may be the betatron acceleration caused by the radial inward diffusion of outer radiation belt electrons, as in the Earth's radiation belt (Allison & Shprits, 2020; Boyd et al., 2018; Chen et al., 2007), plasma injection and/or magnetic compression events (Bolton et al., 1997; Cowley & Bunce, 2003), and magnetic reconnection (Louarn et al., 2014). In general, it is expected that these processes lead to the formation of a loss-cone electron distribution. Indeed, for planetary magnetospheres, such as the Earth, Saturn, or Jupiter, the electrons trapped in the dipolar magnetic field will experience a loss by the mirror force.

Menietti et al. (2020) presented a survey of low-latitudinal whistler mode intensity, including an example of moderate chorus near and within a chorus source region, which took place on 3 November 2019. The electron phase space distribution showed a narrow, weak loss cone, after averaging the data over ∼30 s to improve the quality of the plot. In addition, there appears to be a weak electron "butterfly" pitch-angle distribution centered near pitch angles of 45° and 130° (Sibeck et al., 1987; Xiong et al., 2017). Our focus, however, is on the losscone, which presumably is the primary source of whistler chorus wave excitation. Returning to the overview of the event discussed in detail by Menietti et al. (2020), the wave excitation is seen to take place over a time scale of hours, and the dynamic spectrum indicates that the chorus emission occurs below the half-cyclotron frequency,  $f_{cv}/2$ , down to approximately the lower-hybrid frequency,  $f_{lb}$ , with a generally downward shifting frequency pattern (Note tat  $f_{lh} \sim 160$  Hz at this time, and is off the scale of the spectrogram). This article will focus on this event in order to provide a qualitative theoretical interpretation within the framework of quasilinear theory of the whistler instability excited by the loss-cone distributed electrons. However, in order to simplify the analysis, we will not model the butterfly pitch-angle feature, but rather, we will simplify by adopting the loss-cone distribution function. Even though the basic nature of a wide variety of plasma instabilities is widely discussed in the plasma physics literature, most of the discussions are based on linear theory. As such, one cannot reproduce the dynamic spectrum of the waves, nor address the relaxed state of the particle distribution. Direct numerical simulations can be attempted, but they are computationally costly. In the article, we will thus employ an efficient quasilinear analysis, which has not been applied to the Jovian plasma waves before. We will first discuss the general theoretical formalism in the subsequent section, and the application will be made to the said event in the section that follows. As it will become evident, the theoretically constructed dynamic spectrum of the whistler mode chorus emission shows a rather remarkable agreement with observations. We should note that the quasilinear transport equation widely employed in the radiation belt physics to discuss the electron acceleration and loss, plus the radial transport, is not self consistent in that, the wave intensity is modeled. In such a model, the waves do not evolve in time (Horne et al., 2008; Reeves et al., 2013; Shprits et al., 2012, 2015). In contrast, the quasilinear kinetic theory to be discussed subsequently, computes the wave spectrum self-consistently.

The organization of this article is as follows: In Section 2 we present a brief but self-contained description of the quasilinear theory of whistler instability driven by the loss-cone electron distribution. In Section 3 numerical analysis is carried out and connections with the Juno observation, particularly, the 3 November 2019 event, is made. Finally Section 4 concludes the article, where we discuss the implications of the work as well as the future research directions.

YOON ET AL. 2 of 17



## 2. Quasilinear Theory of Whistler Instability Driven by an Electron Loss-Cone Distribution

In this section we discuss the whistler instability excited by the electron loss-cone distribution and its quasilinear saturation process. We begin with a model of electron distribution function. In the present strategy we model the dynamical evolution of electron distribution function by assuming an analytical form of phase space distribution. Such a model, which can be thought of as the forced self-similar solution of the quasilinear kinetic equation, is assumed to dynamically evolve by virtue of the time-variation of underlying parameters that define the model. This is, of course, a short-cut method that replaces the actual solution of the velocity space diffusion equation, but such a "velocity-moment-based" quasilinear theory was shown to be quite successful when compared against the particle-in-cell (PIC) code simulation—for instance, in modeling the time evolution of various temperature anisotropy-driven instabilities in the solar wind and the magnetosphere (Lee, Lee, et al., 2018; Seough et al., 2014, 2015) as well as the dynamical evolution of magnetospheric Bernstein mode and whistler-mode instabilities driven by a ring distribution of electrons (Lee, Yoon, et al., 2018; Yoon et al., 2019). This method must be guided by physical insight, but as long as the self-similar modeling of the distribution function is done judiciously, the result was proven to be quite valid, as evidenced from the above-referenced comparative studies of various instabilities. In short, we will adopt the same approach in the present analysis.

The net electron distribution function is assumed to be made of a background of relatively cold electrons and an energetic population of loss-cone distributed electrons. Our assumption is that the hot electrons are primarily responsible for the excitation of the whistler instability. The role of background cool electrons is for supporting the whistler mode waves in the plasma. The free energy for the instability comes from the effective temperature anisotropy provided by the loss cone. Energetic electrons trapped within the dipole magnetic field in Jupiter's magnetosphere naturally possess the loss-cone feature. Once the instability is excited, we expect the empty loss cone to be filled, thereby removing the source of instability. Thus, we expect that the most important factor in the time evolution of the distribution function in response to the wave excitation is loss-cone filling by pitch-angle diffusion. Guided by such an expectation we model the energetic (or hot) electrons by (Menietti et al., 2016; Yoon et al., 1998)

$$f(\mathbf{u}) = \frac{n_h}{n_0} N \left( 1 + \frac{u^2}{\kappa \alpha^2} \right)^{-\kappa - 1} \left( \tanh \frac{\mu + \mu_0}{\delta} - \tanh \frac{\mu - \mu_0}{\delta} + \Delta \right),$$

$$N = \frac{1}{\pi^{3/2} \alpha^3 A} \frac{\Gamma(\kappa + 1)}{\kappa^{3/2} \Gamma(\kappa - 1/2)},$$

$$A = \frac{1}{2} \int_{-1}^{1} dx \left( \tanh \frac{x + \mu_0}{\delta} - \tanh \frac{x - \mu_0}{\delta} + \Delta \right),$$
(1)

where  $\mathbf{u} = \mathbf{p}/(mc) = \mathbf{v}/c$  denotes the dimensionless velocity in the non-relativistic formalism,  $\mu = u_{\parallel}/u$  denotes the cosine of the pitch angle, defined with respect to the ambient magnetic field,  $\parallel$  representing direction along the ambient magnetic field, and  $\alpha^2 = 2$   $T/mc^2$  denotes the normalized electron temperature for the energetic component. Here,  $n_{\rm h}/n_0$  designates the ratio of hot versus background electron number densities. The loss-cone angle is defined via the parameter  $\mu_0 = \cos\theta_L$ , where  $\theta_L$  stands for the loss-cone angle. The quantity  $\delta$  is a parameter associated with the smoothness of the loss cone boundary, which we do not vary. The parameter  $\kappa$  is also a fitting parameter associated with the energetic electrons, which is also considered fixed. In Equation 1  $\Gamma(x)$  is the gamma function. The effective temperature or the velocity spread is defined via  $\alpha$ , which is loosely related to thermal speed. The normalization constant N is calculated such that  $f(\mathbf{u})$  is normalized to unity,  $\int d\mathbf{u} f(\mathbf{u}) = 1$ .

The energetic electrons could undergo a mild heating or cooling in response to the whistler mode excitation, but we expect that the most important dynamical change will be associated with the loss-cone fill factor  $\Delta$ . Thus, in our model the most important parameter is  $\Delta$ , which controls the degree of emptiness associated with the loss cone distribution. Initially, this parameter is set equal to zero, but as the whistler instability is excited and proceeds toward saturation, we will self-consistently calculate the time variation of  $\Delta$  so that this parameter will

YOON ET AL. 3 of 17



increase from the initial value of zero to a finite value. Although we expect that the most important dynamical factor is the time evolution of  $\Delta$ , we also self-consistently calculate the change in thermal spread  $\alpha$ , although as we shall see, the change in this parameter is rather minimal. In order to help us determine the time evolutions of  $\alpha$  and  $\Delta$ , it is useful to calculate the following moments of the hot loss-cone electrons,

$$\int d\mathbf{u}u^2 f(\mathbf{u}) = \frac{n_h}{n_0} \frac{\kappa}{\kappa - 3/2} \frac{3\alpha^2}{2},$$

$$\int d\mathbf{u}\mu^2 f(\mathbf{u}) = \frac{n_h}{n_0} \frac{B}{A},$$

$$B = \frac{1}{2} \int_{-1}^1 dx x^2 \left( \tanh \frac{x + \mu_0}{\delta} - \tanh \frac{x - \mu_0}{\delta} + \Delta \right),$$
(2)

from which we may obtain the dynamical evolution equations for  $\alpha$  and  $\Delta$ ,

$$\frac{d\alpha}{dt} = \frac{n_0}{n_h} \frac{\kappa - 3/2}{\kappa} \frac{1}{3\alpha} \int d\mathbf{u} u^2 \frac{\partial f(\mathbf{u})}{\partial t},$$

$$\frac{d\Delta}{dt} = \frac{n_0}{n_h} \frac{3A^2}{A - 3B} \int d\mathbf{u} \mu^2 \frac{\partial f(\mathbf{u})}{\partial t}.$$
(3)

So, as one may appreciate, the dynamics of the hot loss-cone electron distribution function is determined implicitly by the time rate of change in the  $\alpha$  and  $\Delta$  parameters, which in turn, depends on the time rate of change in the distribution function,  $\partial f(\mathbf{u})/\partial t$ , which will be determined by the quasilinear particle kinetic equation. As is well known, the quasilinear particle equation is coupled to the wave kinetic equation. In order to discuss the self-consistent particle and wave kinetic equation under the quasilinear approximation, we next discuss the linear wave dispersion relation and growth rate.

The cold background plasma supports the whistler mode waves, whose dispersion relation is given by Stix (1992) and Melrose (1986)

$$\omega = \Omega_e \cos \theta \frac{c^2 k^2 / \omega_{pe}^2}{1 + c^2 k^2 / \omega_{pe}^2}.$$
 (4)

here,  $\theta$  is the wave propagation angle and k is the wave number. Note that perpendicular and parallel wave numbers, defined with respect to the direction of the ambient magnetic field, are given by  $k_{\perp} = k \sin \theta$  and  $k_{\parallel} = k \cos \theta$ , respectively. The (quasi) linear growth rate for the whistler mode waves is given for, a general hot electron distribution function f, as (Lee, Yoon, et al., 2018; Melrose, 1986)

$$\gamma = \frac{\pi}{2} \frac{(\Omega_e \cos\theta - \omega)^2}{\Omega_e \cos\theta} \int d\mathbf{v} \, v_\perp^2 \sum_{n=-\infty}^{\infty} \left[ \left( \frac{\omega^2 \sin^2\theta + n\Omega_e(\Omega_e \cos\theta - \omega)}{(\Omega_e \cos\theta - \omega)\Omega_e \cos\theta} \right) \frac{J_n(b)}{b} + J'_n(b) \right]^2 \\
\times \delta(\omega - n\Omega_e - kv_\parallel \cos\theta) \left( \frac{n\Omega_e}{v_\perp} \frac{\partial}{\partial v_\perp} + k \cos\theta \frac{\partial}{\partial v_\parallel} \right) f, \qquad b = \frac{kv_\perp \sin\theta}{\Omega_e},$$
(5)

where f denotes the hot loss-cone electron distribution function (Equation 1), and  $\omega$  is given by the whistler wave dispersion relation (Equation 4). In Equation 5,  $J_n(b)$  and  $J'_n(b)$  denote the Bessel function of the first kind of order n and its derivative with respect to the argument, respectively. By substituting the model distribution (Equation 1) we obtain, after some straightforward mathematical manipulations, the following expression for the whistler wave growth rate:

YOON ET AL. 4 of 17

$$\Gamma_{\mathbf{q}} = \frac{\gamma}{\Omega_{e}} = \frac{n_{h}}{n_{0}} \frac{\pi^{1/2}}{A} \frac{\Gamma(\kappa + 1)}{\kappa^{3/2} \Gamma(\kappa - 1/2)} \frac{q_{\parallel}}{q(1 + q^{2})^{3} r \alpha}$$

$$\times \int_{0}^{\infty} dx x^{3} \sum_{n=-\infty}^{\infty} \left[ \left( \frac{q^{2} q_{\perp}^{2}}{1 + q^{2}} + \frac{nq}{q_{\parallel}} \right) \frac{J_{n}(b)}{b} + J'_{n}(b) \right]^{2}$$

$$\times \left( -\frac{\kappa + 1}{\kappa} \frac{2q(\tanh \zeta_{n} - \tanh \xi_{n} + \Delta)}{(1 + u_{n}^{2}/\kappa)^{\kappa+2}} + \frac{qy_{n} - (1 + q^{2})r\alpha u_{n}^{2}}{\delta u_{n}^{3}} \frac{\tanh^{2} \zeta_{n} - \tanh^{2} \xi_{n}}{(1 + u_{n}^{2}/\kappa)^{\kappa+1}} \right), (6)$$

$$b = q_{\perp} r \alpha x, \qquad y_{n} = \frac{qq_{\parallel} - n(1 + q^{2})}{(1 + q^{2})q_{\parallel} r \alpha}.$$

$$u_{n} = (x^{2} + y_{n}^{2})^{1/2}, \qquad \mu_{n} = \frac{y_{n}}{(x^{2} + y_{n}^{2})^{1/2}}, \qquad \zeta_{n} = \frac{\mu_{n} + \mu_{0}}{\delta}, \qquad \xi_{n} = \frac{\mu_{n} - \mu_{0}}{\delta},$$

where

$$q = \frac{ck}{\omega_{pe}}, \qquad r = \frac{\omega_{pe}}{\Omega_e}, \qquad z_{q} = \frac{\omega}{\Omega_e} = \frac{qq_{\parallel}}{1+q^2},$$
 (7)

and  $q_{\perp} = q \sin \theta$  and  $q_{\parallel} = q \cos \theta$  denote the perpendicular and parallel components of the normalized wave vector, respectively, in cylindrical coordinate. Note that the parameter  $r\alpha$  is the square root of electron beta,  $r^2\alpha^2 = \beta_e = 8\pi n_0 T_e/B_0^2$ .

The dynamical equation of velocity moments of f, that is, Equation 3 depends on the time evolution of f, which is given by the quasilinear particle kinetic equation, which is given in general form by (Melrose, 1986)

$$\frac{\partial f}{\partial t} = \frac{1}{v^2} \frac{\partial}{\partial v} \left[ v^2 (1 - \mu^2) \left( D_{vv} \frac{\partial f}{\partial v} - D_{v\mu} \frac{1}{v} \frac{\partial f}{\partial \mu} \right) \right] 
- \frac{1}{v} \frac{\partial}{\partial \mu} \left[ (1 - \mu^2) \left( D_{v\mu} \frac{\partial f}{\partial v} - D_{\mu\mu} \frac{1}{v} \frac{\partial f}{\partial \mu} \right) \right], 
\left( D_{vv} \right) 
\left( D_{v\mu} \right) = \frac{\pi e^2}{m_e^2} \int d\mathbf{k} \sum_{n=-\infty}^{\infty} \delta(\omega - k_{\parallel} v \mu - n\Omega_e) |\mathbf{V}_n \cdot \mathbf{e}^*(\mathbf{k})|^2 \left( \mu - k_{\parallel} v / \omega \right)^2 \right) \langle \delta E^2 \rangle_{\mathbf{k}}, 
\left( V_n^* \cdot \mathbf{e}(\mathbf{k}) \right)^2 = \frac{1}{1 + K^2 + T^2} \left| \frac{\omega}{\Omega_e} \left[ K \frac{k_{\perp}}{k} + T \left( \frac{k_{\parallel}}{k} - \frac{k}{k_{\parallel}} \frac{\omega - n\Omega_e}{\omega} \right) \right] \frac{J_n(b)}{b} - J_n'(b) \right|^2, 
b = \frac{k_{\perp} v (1 - \mu^2)^{1/2}}{\Omega_e}.$$
(8)

here, we have represented the right-hand side of the kinetic equation in a spherical velocity coordinate system. In Equation 8 *T* and *K* are the coefficients that define the unit electric field vector, or equivalently, the polarization vector (Melrose, 1986). For the whistler mode these are given by (Lee, Yoon, et al., 2018)

$$T = -1, K = -\frac{(1+q^2)q_{\perp}}{q_{\parallel}},$$
 (9)

so that we may write Equation 8, in appropriate dimensionless quantities and variables, as

YOON ET AL. 5 of 17

$$\frac{\partial f}{\partial \tau} = \frac{1}{u^{2}} \frac{\partial}{\partial u} \left[ u^{2} (1 - \mu^{2}) \left( D_{uu} \frac{\partial f}{\partial u} - D_{u\mu} \frac{1}{u} \frac{\partial f}{\partial \mu} \right) \right] 
- \frac{1}{u} \frac{\partial}{\partial \mu} \left[ (1 - \mu^{2}) \left( D_{u\mu} \frac{\partial f}{\partial u} - D_{\mu\mu} \frac{1}{u} \frac{\partial f}{\partial \mu} \right) \right], 
\left( D_{uu} \right) 
\left( D_{\mu\mu} \right) 
= \frac{\pi}{r^{2}} \int \frac{d\mathbf{q}}{q^{2}} z_{\mathbf{q}}^{2} \mathcal{H}_{\mathbf{q}} W_{\mathbf{q}} \sum_{n=-\infty}^{\infty} \delta(z_{\mathbf{q}} - rq_{\parallel}u\mu - n) \left| \mathcal{M}_{n} \frac{J_{n}(b)}{b} + J'_{n}(b) \right|^{2} \left( \frac{1}{(\mu - rq_{\parallel}u/z_{\mathbf{q}})^{2}} \right), 
\mathcal{H}_{\mathbf{q}} = \frac{q_{\parallel}^{2}}{2q_{\parallel}^{2} + (1 + q^{2})^{2} q_{\perp}^{2}}, \qquad \mathcal{M}_{n}(\mathbf{q}) = \frac{q^{2} q_{\perp}^{2}}{1 + q^{2}} + \frac{nq}{q_{\parallel}}, \qquad b = rq_{\perp}u(1 - \mu^{2})^{1/2},$$
(10)

where  $W_{\mathbf{q}}$  designates the dimensionless magnetic field energy density associated with the whistler mode waves, and  $\tau$  represents the normalized time,

$$W_{\mathbf{q}} d\mathbf{q} = \frac{\delta B_{\mathbf{k}}^2 d\mathbf{k}}{B_0^2}, \qquad \tau = \Omega_e t. \tag{11}$$

note that the system of equations is closed by the self-consistent wave kinetic equation,

$$\frac{\partial W_{\mathbf{q}}}{\partial \tau} = 2\Gamma_{\mathbf{q}} W_{\mathbf{q}}. \tag{12}$$

Inserting Equation 10 into the right-hand side of Equation 3 one obtains the set of equations that describe the quasilinear evolution of the loss-cone electron distribution and the whistler mode wave intensity. Let us recapitulate the final set of equations for the sake of completeness,

$$\frac{d\alpha}{d\tau} = -\frac{n_0}{n_h} \frac{\kappa - 3/2}{\kappa} \frac{4}{3r^2 \alpha} \int d\mathbf{q} (1+q^2) \mathcal{H}_{\mathbf{q}} \Gamma_{\mathbf{q}} W_{\mathbf{q}},$$

$$\frac{d\Delta}{dt} = \frac{n_0}{n_h} \frac{12A^2}{A - 3B} \int d\mathbf{q} (1+q^2) \mathcal{H}_{\mathbf{q}} \eta_{\mathbf{q}} W_{\mathbf{q}},$$
(13)

where the wave kinetic equation is given by Equation 12, and the quantity  $\eta_{\mathbf{q}}$  is defined by

$$\eta_{\mathbf{q}} = \frac{n_{h}}{n_{0}} \frac{\pi^{1/2}}{A} \frac{\Gamma(\kappa + 1)}{\kappa^{3/2} \Gamma(\kappa - 1/2)} \frac{q_{\parallel}}{q(1 + q^{2})^{3} (r\alpha)^{3}} \\
\times \int_{0}^{\infty} dx x \sum_{n} \mu_{n} (1 - \mu_{n}^{2}) \left( \mu_{n} - r\alpha u_{n} \frac{1 + q^{2}}{q} \right) \left| \mathcal{M}_{n} \frac{J_{n}(b)}{b} + J'_{n}(b) \right|^{2} \\
\times \left( -\frac{\kappa + 1}{\kappa} \frac{2q(\tanh \zeta_{n} - \tanh \zeta_{n} + \Delta)}{(1 + u_{n}^{2}/\kappa)^{\kappa + 2}} + \frac{qy_{n} - (1 + q^{2})r\alpha u_{n}^{2}}{\delta u_{n}^{3}} \frac{\tanh^{2} \zeta_{n} - \tanh^{2} \zeta_{n}}{(1 + u_{n}^{2}/\kappa)^{\kappa + 1}} \right), \tag{14}$$

and where the various quantities are defined exactly as in Equation 6.

### 3. Numerical Analysis and Comparison With Observation

As an example, we solved the set of equations which we have derived thus far, namely, the velocity moment kinetic (Equation 3), wave kinetic (Equation 12), together with the instantaneous growth rate (Equation 5), or its normalized form (Equation 6), for a set of input parameters corresponding to  $n_h/n_0 = 0.1$ ,  $\omega_{pe}/\Omega_e = 10$ ,  $\mu_0 = 0.99$ ,  $\delta = 0.01$ , and  $\kappa = 2$ , which are invariant parameters, and the initial values of  $\alpha(0) = 0.1$  and  $\Delta(0) = 0$ . The choice of these parameters requires some explanations. The relative number density of the energetic electrons with respect to the background electrons is not so easy to determine on the basis of spacecraft measurement. However, in general, we expect this number to be at most 10%, hence, our choice. The ratio of plasma-to-electron gyro-frequency,  $f_{pe}/f_{ce} = \omega_{pe}/\Omega_e$  is relatively straightforward to determine. According to Menietti et al. (2020),

YOON ET AL. 6 of 17

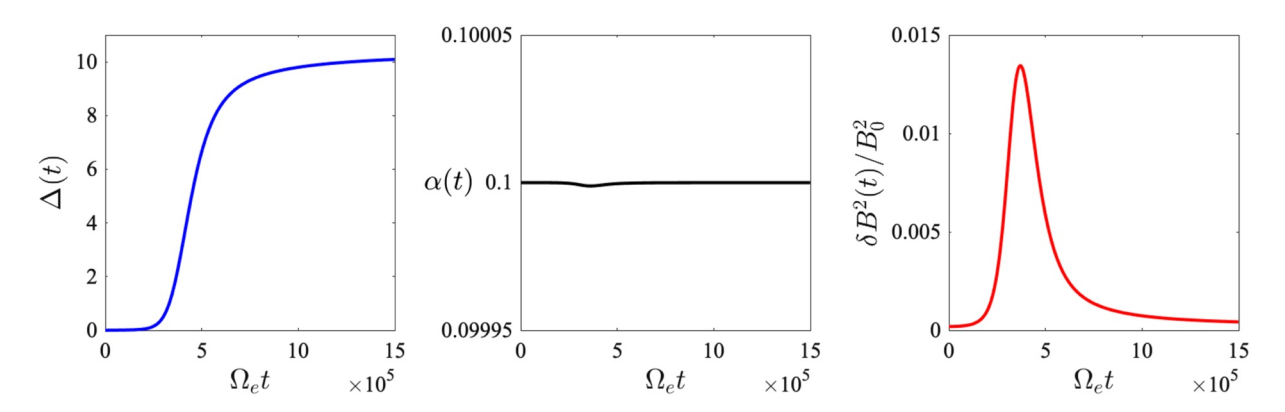


Figure 1. Dynamical evolution of parameters  $\Delta$  (left) and  $\alpha$  (middle), which define the loss-cone phase space distribution (1), together with the normalized whistler mode wave magnetic field energy density (right), for input parameters  $n_h/n_0 = 0.1$ ,  $\omega_{pe}/\Omega_e = 10$ ,  $\mu_0 = 0.99$ ,  $\delta = 0.01$ , and  $\kappa = 2$ , which are invariant quantities, and for initial values of  $\alpha(0) = 0.1$  and  $\Delta(0) = 0$ .

the 3 November 2019 event is characterized by the upper-hybrid frequency of the order tens of kHz, while the electron cyclotron frequency is identified to be in the frequency range of a few kilohertz. Consequently,  $f_{ne}/f_{ce}$  is easily identified to be of the order 10 or so, or more precisely,  $f_{ce}/f_{pe} \sim 8.5$ . The loss-cone angle  $\theta_L = \cos^{-1}\mu_0$  is not so straightforward to determine. The energetic particle detector Jovian Auroral Distribution Experiment (JADE) (Allegrini et al., 2017, 2020; McComas et al., 2017) measures electron energies in the range of tens of electronvolt up to hundreds of kiloelectronvolt, but the pitch angles are averaged over all energies, with the resolution of a few degrees. In the equatorial regions of the Jovian magnetosphere we expect the loss-cone angles to be quite low, of only a couple of degrees. Such a narrow loss-cone angle is not directly observed at this time by JADE, because of the instrument resolution and the averaging of the contour plot. We thus choose  $\mu_0 = 0.99$ , which closely matches the expected value of a couple of degrees of loss-cone angle, despite the fact that the instruments may not resolve these angles. The parameter  $\delta$ , which smooths the loss-cone edge in the velocity space distribution, is entirely arbitrary, but we choose a fixed value of  $\delta = 0.01$ . We have varied this parameter, for instance,  $\delta = 0.001$ –0.05, but have found no significant difference in the outcome. Finally, the kappa parameter of  $\kappa = 2$ is also somewhat artificial, but such a value seems to be typical of planetary magnetospheric environment—see, for example, Eyelade et al. (2021) for the case of Earth's magnetosphere and (Menietti, Yoon, et al., 2019) for Saturnian example. The thermal energy associated with the energetic electrons is roughly given by  $E/(m_cc^2)$  $[\kappa/(\kappa - 3/2)](3\alpha^2/2)$ . The initial choice of  $\alpha(0) = 0.1$  thus corresponds to approximately 5 keV thermal energy. The loss-cone fill factor is initially set equal to zero,  $\Delta(0) = 0$ . In summary, the input parameters are  $n_\nu/n_0 = 0.1$ ,  $\omega_{n'}/\Omega_e = 10, \mu_0 = 0.99, \delta = 0.01, \kappa = 2, \alpha(0) = 0.1, \text{ and } \Delta(0) = 0.$  We deem that these are appropriate parameters to characterize the 3 November 2019 event. In the Appendix, we consider further parametric studies by varying some of the key input parameters.

The result of quasilinear velocity moment calculation based upon the set of input parameters described above is shown in Figure 1. The left-hand panel plots the time evolution of  $\Delta(t)$ . Note that  $\Delta$  increases from its initial value of 0 to ~10 toward the end of computation. In our numerical scheme, we find that the quasi saturation is achieved over a very long inverse electron cyclotron period,  $t_{\rm sat} \sim 10^6 \Omega_e$ . Given that  $f_{\rm ce}$  is of the order of kHz, this time scale corresponds to approximately an hour, which is consistent with observation. The loss-cone filling, or the increase in  $\Delta$ , is the result of pitch angle diffusion, which the present model encapsulates. The middle panel, which plots the time evolution of  $\alpha$ , shows that the pitch-angle diffusion process does not affect the thermal energy. Finally, the time evolution of the normalized whistler mode wave energy density,  $\delta B^2(t)/B_0^2 = \int d\mathbf{q} W_{\mathbf{q}}$ , is plotted on the right-hand panel. Note that the whistler mode magnetic field energy density first undergoes an exponential increase as a result of the instability excitation, and is followed by the saturation. Beyond the saturation stage, however, the wave energy density is gradually reabsorbed by the hot electrons, but since the wave energy density is generally low, which owing to the narrow loss-cone angle, and thus, low free energy source, the electron heating is minimal, if at all. Note that near the quasilinear saturation stage the electron thermal energy is decreased slightly, but beyond the saturation stage, thermal energy level recovers almost to its initial value.

We may reconstruct the underlying loss-cone model distribution (Equation 1) at various instants along the dynamic evolution based upon  $\alpha(t)$  and  $\Delta(t)$  evaluated from the velocity moment calculation, as shown in Figure 1.

YOON ET AL. 7 of 17

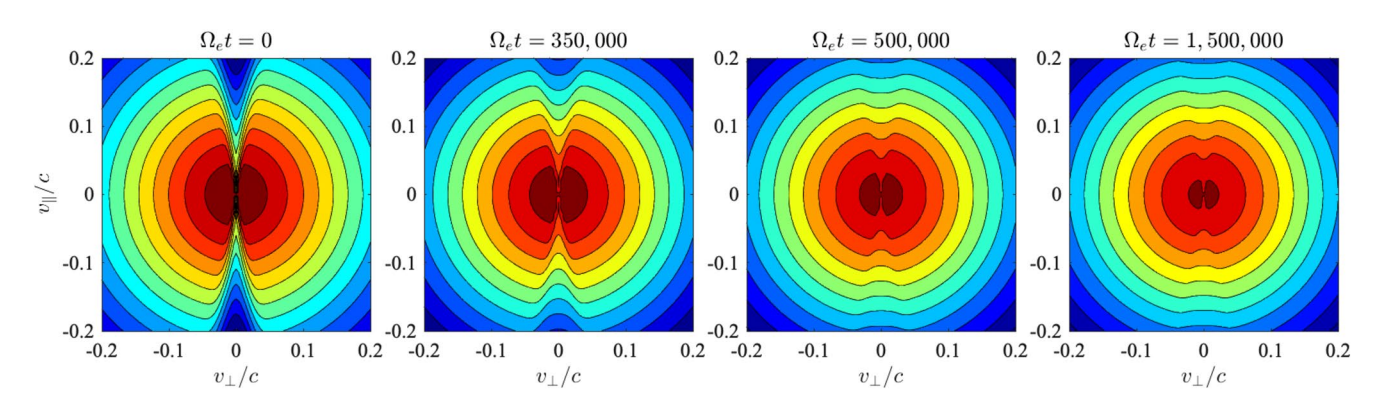


Figure 2. Snapshot of model loss-cone distribution function  $f(v_{\perp}, v_{\parallel})$  versus  $u_{\perp} = v_{\perp}/c$  and  $u_{\parallel} = v_{\parallel}/c$ , at four different time steps corresponding to  $\tau = \Omega_e t = 0, 3.5 \times 10^5, 5 \times 10^5,$ 

In Figure 2 we have thus plotted the velocity distributions functions at  $\tau = \Omega_e t = 0$ ,  $3.5 \times 10^5$ ,  $5 \times 10^5$ , and  $1.5 \times 10^6$ . Starting from the almost empty loss cone for  $\mu < \mu_0$ , the loss-cone is seen to gradually fill up. The model (Equation 1) is thus quite a reasonable representation of the anticipated physical process. Similar models of the whistler mode instability involving the bi-Maxwellian model (Lee, Yoon, et al., 2018) and ring/partial shell distribution (Yoon et al., 2019) have successfully been tested against the PIC simulation. Based upon these prior successes, we believe that the present velocity moment-based modeling of the loss-cone whistler instability is appropriate for the situation at hand. The present method is particularly efficient given the fact that the entire quasilinear saturation process takes place in an extremely long interval from the theoretical perspective, that is,  $t_{\rm sat} \sim 10^6 \Omega_e^{-1}$  or longer. Such a weak instability and long saturation time make the direct numerical PIC simulation quite impractical, and even the direct numerical solution of the quasilinear diffusion Equation 10 quite inefficient. Note that the basic methodology of partial differential equation solver is available to us and has been applied in different applications—see, for example, Tigik et al. (2016). As a consequence, we could have attempted to solve the basic set of equations by such means, but because of the basic nature of the problem, we deemed that it is much more practical to simply model the underlying distribution function based upon intuition, and proceed with the velocity moment quasilinear calculation.

Note that the model distribution function at quasi saturation stage of  $\Omega_{\rm e}t = 1.5 \times 10^6$  bears some superficial similarities with typical measurements in the Jovian magnetospheric environment. The phase space distribution

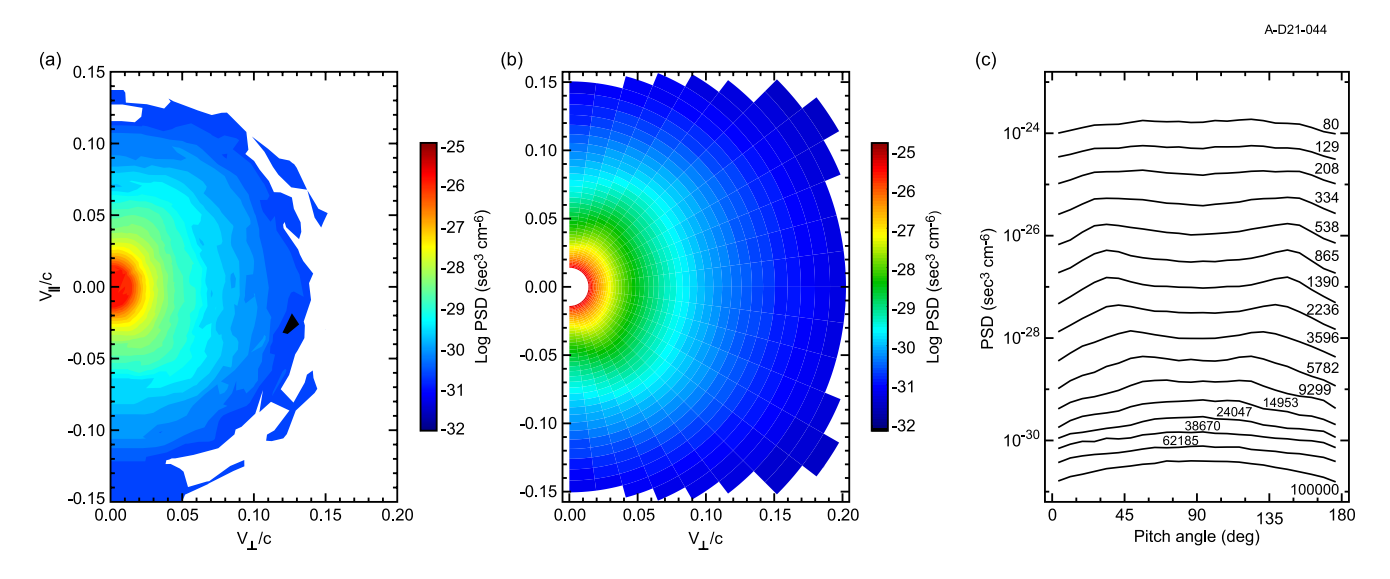


Figure 3. Phase space distribution (PSD) from JADE for 3 November 2019. (a) Contour of the distribution obtained at 12:55:01.7 (near the source region shown in Figure 4). (b) High resolution binning of the PSD averaged over 30 s around 12:55:01. (c) About 30-s averaged PSD versus pitch angle at each energy step ranging from 50 eV to 100 keV as labeled.

YOON ET AL. 8 of 17

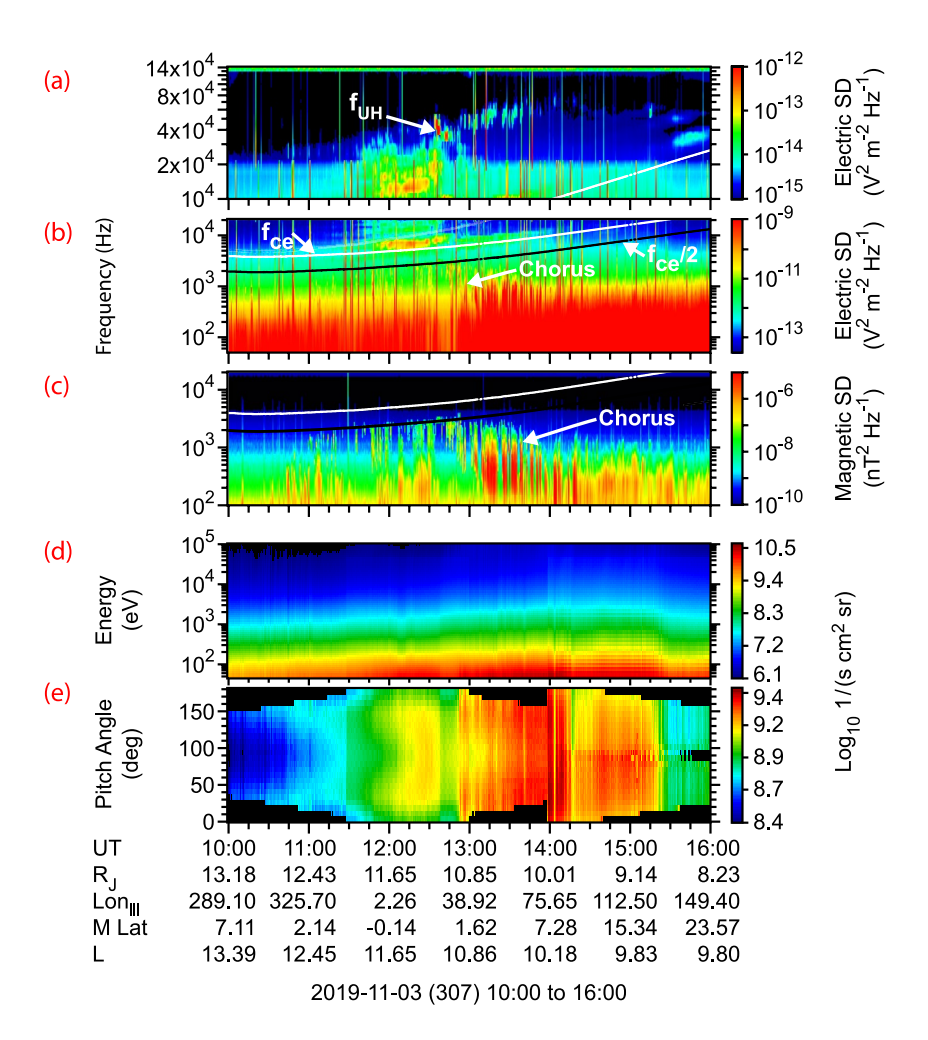


Figure 4. Multi-instrument display pf Waves and JADE data taken on 3 November 2019, during a moderate episode of whistler mode chorus emission for orbit PJ23.

from JADE for 3 November 2019 is displayed in Figure 3. Figure 3a is a contour of the distribution obtained at 12:55:01.7 during the observation of Jovian chorus near the source region shown in Figure 4. Figure 3b is a high resolution binning of the PSD that is an average over 30 s around 12:55:01. Figure 3c shows the 30-s averaged PSD versus pitch angle displayed in a line plot at each energy step ranging from 50 eV to 100 keV. Figure 3c indicates a roughly pancake distribution for low energies (<200 eV), almost butterfly for mid energies (~200 eV to ~9 keV), and pancake for higher energies (>9 keV). As Figure 3 shows, the measured electron distribution does not show a well-defined loss cone, because the instrument resolution is not high enough. This may lead to a misleading conclusion if one is to rely solely on the linear theory. However, as Figure 2 demonstrates, the saturated stage of the electrons simply may mean a relaxed state of the wave excitation process, so that the coexistence of quasi-isotropic phase space distribution and enhanced whistler wave intensity are not necessarily inconsistent. The present quasilinear analysis is useful in this regard.

Menietti et al. (2020) showcases a typical event that took place on 3 November 2019. Figure 4 is a reproduction from the same article, where the Juno Waves instrument (Kurth et al., 2017) and JADE collected data during a moderate episode of whistler-mode chorus emission observed on orbit PJ23, on 3 November 2019. The location of Juno was between 8.2 and  $13.2\,R_J$  covering the magnetic latitudes  $\sim 0 < \lambda < 23.6^\circ$ . Figures 4a–4c plot frequency-time dynamic spectrograms from waves. Spectral densities taken from LFR-hi and LFR-lo electric are plotted in the Figures 4a and 4b, and LFR-B magnetic wave spectral density is plotted Figure 4c. As noted by Menietti et al. (2020), chorus emission begins just before 11:00 UT and becomes most intense just after 13:00 UT where it extends to low frequencies and continues until  $\sim 14:25$ . Note that the whistler mode chorus is generally constrained below  $f_{ce}/2$  and gradually downshifts in frequency over time. Figures 4a and 4b also show electrostatic

YOON ET AL. 9 of 17



cyclotron harmonic waves above  $f_{\rm ce}$  and the upper-hybrid emission, but these are beyond the scope of the present analysis. Electron data from JADE are shown in Figures 4d and 4e in the form of an energy-time spectrogram of differential flux and pitch-angle-time spectrogram of differential flux. The example in Figure 4 is a "moderate" case of chorus observed at Jupiter by Juno, but the event is observed over space and time. Juno observes chorus each time it passes through this region of the Jovian magnetosphere. The loss cone distribution is believed to be present throughout this region of chorus growth, although the growth of the waves obviously changes the distribution with loss cone filling occurring as a result of instability excitation and saturation. Plasma wave polarization and wave normal angle are not available on the Juno mission, since the Juno Waves instrument only has a single dipole antenna and a single search coil. This contrasts to the terrestrial chorus waves where normal angle with latitude are observed (cf. Gao et al., 2016).

Again, as noted by Menietti et al. (2020), there appears to be a positive correlation between the electrons and the chorus emission in that the differential flux increases between  $\sim$ 12:40 and 14:15 UT, as the chorus intensity also increases, and the pitch angle distribution develops from butterfly to trapped-like (peaking near 90°) and finally to isotropic in about 1 hr. All this occurs, however, over a range of about  $1R_p$ , 7° magnetic latitude, and about 40° system III longitude. So we are observing temporal and spatial changes that will take careful interpretation as we discuss below. Wave scattering is occurring throughout the region of chorus observations in Figure 4. The pitch angle observations of Figure 4e indicate significant changes in the phase space distribution. Black indicates no data, and loss cones are not easily visible, but near 12:30 the distribution is more pancake, while from about 12:45 to 13:00 it is "butterfly" as in Figure 3. Near isotropic distributions are dominant from about 13:45 to 14:25. But each observation is from a different location. The loss cone is very narrow at all times, and is quite difficult to observe due to the limits in resolution of the JADE instrument.

As the Juno observation is pertinent to the low-latitude region, the loss cone is expected to be narrow initially. In fact, this has motivated us to model a narrow electron loss-cone distribution function as shown in Figure 2. Despite this, we have succeeded in demonstrating that the whistler mode waves are excited by such a narrow loss-cone electron distribution. A salient feature is that the most intense whistler mode chorus wave emission is seen to take place over a time frame that spans an hour or more. This is quite consistent with the present finding. Note, however, that this statement ignores the fact that during this hour the spacecraft location has changed radial distance, MLat, and longitude by substantial amounts. To accurately model such an effect requires the extension of the present approach to include spatial inhomogeneity effects, which is beyond the scope of the article, and must be considered as part of future research tasks.

The present quasilinear analysis can also be employed in order to understand how the wave propagation characteristics associated with the whistler mode evolve in time. Figure 5 plots the snapshot of wave growth rate superposed over the surface plot of the dispersion relation at different time steps. Top-left panel corresponds to the initial state. The growth rate at t = 0 peaks at an oblique angle, hence, can be characterized as the obliquely propagating whistler mode wave. The basic wave characteristics undergoes some changes for  $\Omega_t t = 3.5 \times 10^5$ (top-right), to  $\Omega_a t = 5 \times 10^5$  (bottom-left), and to  $\Omega_a t = 1.5 \times 10^6$  (bottom-right), which is the final time step of the present numerical calculation, in that the wave amplitude, frequency, peak wavenumber, and propagation angle continually evolve over time. The general trend is that the whistler mode growth remains slightly more quasi perpendicular and the real frequency corresponding to the peak growth rate steadily decreases over time admittedly, this may be difficult to see in Figure 5, but will be more evident in Figure 6. As time progresses, the peak growth rate also monotonically decreases, as the color bar plotted on the right-hand side of each panel indicates—note that the normalized growth rate is plotted in logarithmic color scale. Note that the overall growth rate remains rather low, on the order of  $10^{-5}\Omega_a$  and lower as time progresses. Note also that the final computation time of  $\Omega_0 t = 1.5 \times 10^6$  is not a true saturation time as the growth rate is still finite, albeit extremely low. Note that the Jovian magnetospheric environment is replete with the background magnetic fluctuations, as Figure 4 shows. We have not modeled such an enhanced background noise, but we initialized our quasilinear calculation with a quiescent background. It is possible to include such a noise by incorporating the background fluctuations with the aid of spontaneous emission theory, however, but it is beyond the scope of the article. Note also that ULF waves are present at Jupiter, but they are not the source of chorus emission. They could cause long period oscillations of the chorus or other waves as well. ULF waves have been suggested as a possible source of "quasiperiodic" auroral hiss at Saturn (cf. Menietti, Palmaerts, et al., 2019; Yates et al., 2016). To repeat, this kind of extremely weakly growing instability poses a great challenge to direct numerical simulation or more rigorous

YOON ET AL. 10 of 17

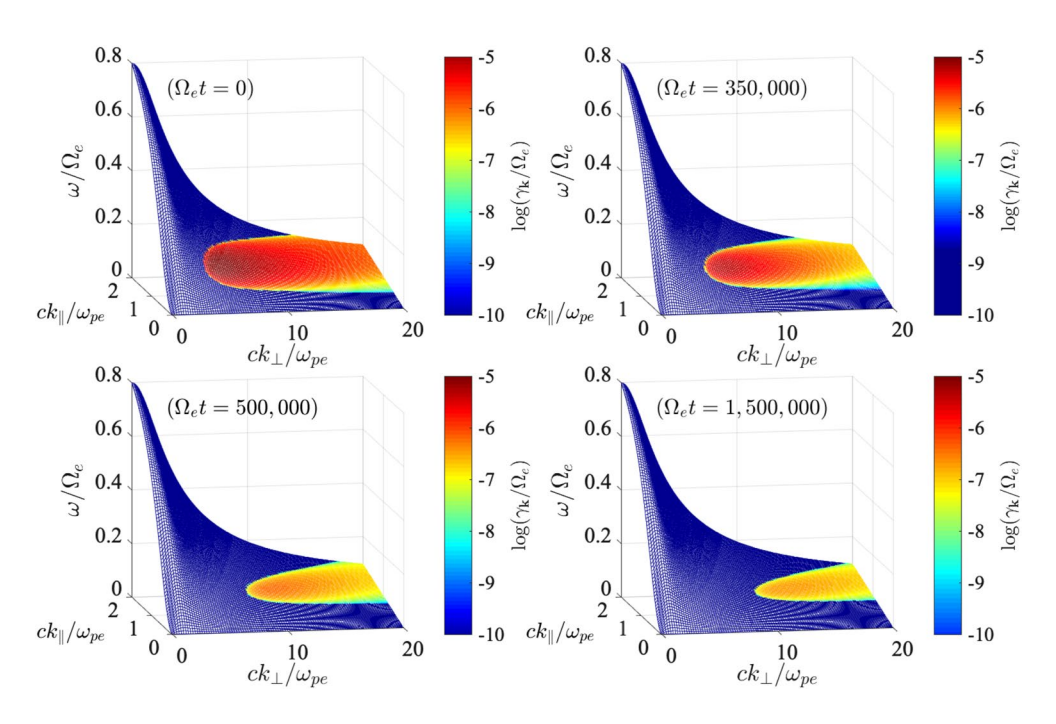
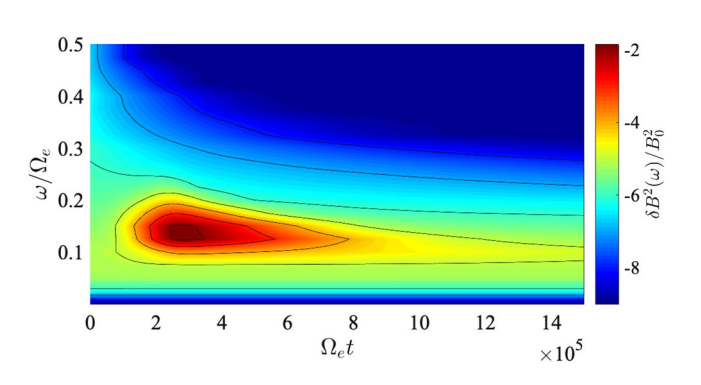


Figure 5. The whistler mode dispersion surface and the instantaneous growth rate  $\Gamma = \gamma_k / \Omega_e$  (in log scale) versus  $q_{\perp} = ck_{\perp}/\omega_{pe}$  and  $q_{\parallel} = ck_{\parallel}/\omega_{pe}$ , superposed as colormap with the color level indicated by the color bar on the right, at four different time steps corresponding to  $\tau = \Omega_e t = 0$ ,  $3.5 \times 10^5$ ,  $5 \times 10^5$ , and  $1.5 \times 10^6$ .

direct numerical calculation of the velocity space diffusion equation, but the present velocity moment scheme represents an efficient means to tackle such a challenge.

In Figure 6 we have replotted the quasilinear theoretical result in a format that can directly be compared with observations. In specific, we have integrated the theoretical whistler mode wave spectrum in wave vectors so that the result is a dynamic spectrum of  $\delta B^2(\omega)/B_0^2$  versus frequency and normalized time. Peak signals in Figure 4c, indicate  $\Delta B^2/B_0^2 \sim 10^7$ -10<sup>8</sup> and peak chorus amplitudes are about 500 pT. Figure 6 indicates  $\Delta B^2/B_0^2 \sim 10^6$ , but Figure 4 is is a spectrogram made while passing through a region of chorus generation, while Figure 6 describes how a point within the source region would develop over time in the absence of plasma injections or precipitation. We caution the readers that the estimate of  $\delta B/B_0$  from the data could be off by an order of magnitude or more. We commented in Menietti et al. (2020) that the electron flux increases during this period are suggestive of an electron injection event having recently occurred. It is interesting to note that the theoretical whistler mode spectrum stays below  $f_{cc}/2$  (or equivalently,  $\Omega_c/2$ ) with the upper envelope of the spectrum gradually decreasing in frequency throughout the entire range of calculation. Note that this is to be expected from quasilinear theory in that, as the electrons lose the free energy, that is, the loss cone filling up, the range of unstable wave numbers shifts to longer



**Figure 6.** Theoretically reconstructed frequency-time spectrogram of the whistler mode chorus wave. The total time scale of  $0 < t < 1.5 \times 10^6 \Omega_e^{-1}$  can be translated to approximately an hour.

wavelength regime, or equivalently, low frequency regime. This compares to the Juno observation, which also shows that the chorus reaches  $f_{\rm ce}/2$  (with the peak intensity remaining well below  $f_{\rm ce}/2$ ) and eventually falling to  $f/f_{\rm ce} \sim 0.1$  after 13:30 in Figure 4c. As such, there is a qualitative (and even to a degree, quantitative) agreement between the theory and the Juno observations. Note that the theoretical time scale of  $0 < t < 1.5 \times 10^6 \Omega_{\rm c} t$ , when translated to actual time, given the typical electron cyclotron frequency of the order approximately kilohertz, corresponds to about an hour or so, which is consistent with observed time period of most intense whistler mode emissions—see Figure 4c. We should note, however, that the duration of approximately an hour refers to the entire period of whistler mode wave excitation, peak intensity, and gradual reduction in intensity until it reaches quasi saturation state. If we consider only the time scale involved with the peak whistler mode intensity, then the estimated time is much shorter, on the order of  $\sim$  =50 s or so. Figure 4c shows that the chorus emission is made of multiple elements. The

YOON ET AL. 11 of 17



estimated time of  $\sim$ 50 s is actually compatible with the observations if we consider the duration of individual whistler mode element rather than the entire period of wave observation. We reiterate that this rough estimate ignores the spatial inhomogeneity effects given that the spacecraft location changes considerably over the time period of  $\sim$  hour. Such a caveat notwithstanding, the present finding implies that the comparison with quasilinear calculation is actually quite favorable. The total duration of the spacecraft data may be made of a large number of individual loss-cone driven whistler mode emission events, but it is interesting to note that the theoretical time scale is in a reasonable agreement with observation in an overall sense. This shows that the present analysis may be relevant for Juno observations, and thus points to further usefulness for other events.

### 4. Discussion

Before we conclude and summarize the article, we consider the impacts of varying input parameters. In the main body of the article we focused our analysis based on one set of input parameters,  $n_{\rm h}/n_0=0.1$ ,  $\omega_{\rm pe}/\Omega_{\rm e}=10$ ,  $\mu_0=0.99$ ,  $\delta=0.01$ ,  $\kappa=2$ ,  $\alpha(0)=0.1$ , and  $\Delta(0)=0$ . In the present section, we consider the sensitivity of the final result, namely, the dynamic spectrum, on variations of some key parameters. Of these,  $\omega_{\rm pe}/\Omega_{\rm e}$  and  $\alpha$  always appear as products,

$$\frac{\omega_{pe}^2}{\Omega_e^2}\,\alpha^2 = \frac{4\pi n_0 T}{B_0^2} = \beta,$$

in the quasilinear theory. As such, variations of one parameter is sufficient for the discussion. Of the two,  $\omega_{re}/\Omega_{e} \sim 10$  is consistent with the 3 November 2019 event. According to Figure 4, JADE instrument indicate the electron energy of not much more than  $\sim$ 5 keV, which corresponds to  $\alpha \sim 0.1$ . Consequently, one should not vary  $\alpha$  too much from this value. We thus vary  $\alpha$  from the reference case of 0.1 (or ~5 keV), to 0.125 (or ~8 keV), and to 0.15 (or ~12 keV, which is already a bit too high). The growth rate is directly proportional to the number density  $n_b/n_0$ , and we made the choice of  $n_b/n_0 = 0.1$  as a rough estimate. Here, we vary  $n_b/n_0$  from the reference case of 0.1, 0.05, and 0.2. The kappa index of  $\kappa = 2$  is a rough estimate, and we do not vary this parameter. It should be noted that the  $\kappa$  value is intimately related to the suprathermal electron energy at the tail of the phase space distribution. Since the free energy source of the whistler mode chorus waves resides in the loss-cone feature associated with the electrons, we pay attention to three key parameters that define the loss-cone. First is the parameter  $\delta$  that defines the sharpness of the loss-cone edge. In the main analysis, we chose  $\delta = 0.01$  and mentioned that the final result does not sensitively depend on the choice of  $\delta$ , but we consider two other cases, namely,  $\delta = 0.005$  and 0.02. For the 3 November 2019 event, where Juno spacecraft measurement was done in the low-latitude region, we noted that the loss-cone angle should be no more than a few (or even a couple of) degrees. Indeed, Figure 3 shows that JADE measurement of energetic electrons hardly shows any loss-cone. Although we interpreted this in terms of the relaxed distribution function as a result of quasilinear relaxation, nevertheless, we may conclude that the loss-cone angle cannot be too large. We vary the loss-cone angle from  $\mu_0 = 0.99$  (or  $\theta_1 = 4^{\circ}$ , the reference case), to  $\mu_0 = 0.98$  (or  $\theta_L = 6^\circ$ ), and to  $\mu_0 = 0.97$  (or  $\theta_L = 7^\circ$ ).

In Figure 7 left-hand panels, we display the dynamic spectrum (from top to bottom) computed for  $\delta=0.005$ ,  $\delta=0.01$  (the reference case), and  $\delta=0.02$ . Notice that the results for all three cases are quite similar. In the second columns (from left) in Figure 7 we consider the loss-cone angle variation, from top to bottom,  $\mu_0=0.99$  (or  $\theta_L=4^\circ$ , the reference case),  $\mu_0=0.98$  (or  $\theta_L=6^\circ$ ), and  $\mu_0=0.97$  (or  $\theta_L=7^\circ$ ). The latter two loss-cone angles, namely,  $\theta_L=6^\circ$  and  $7^\circ$ , are probably unrealistic for 3 November 2019 event. As the wider loss-cone indicates higher free energy, the entire instability and saturation process proceeds faster for higher loss-cone angles. The third columns in Figure 7 depict the dependence on thermal (or kinetic) energy of the loss-cone electrons. Again, it is not surprising that the higher kinetic energies of  $\sim$ 8 and  $\sim$ 12 keV lead to faster evolution, but such are probably unrealistic for the event of interest to us anyway. Finally, the right-hand columns depict the dependence on the density ratio  $n_h/n_0$ . Again, as expected, the lower density ratio leads to a more gradual instability evolution as well as lower saturation wave intensity, and *vice versa*.

We also touch upon the issue of interpreting the single chorus element simulated by the present quasilinear wave analysis and its relation to the observation. The analytical calculation indicates that the evolution of the chorus growth could persist over a period of about an hour, assuming an initial value problem, but the most intense periods could be much shorter. Juno traversed a region where chorus emission is observed and generated at different

YOON ET AL. 12 of 17

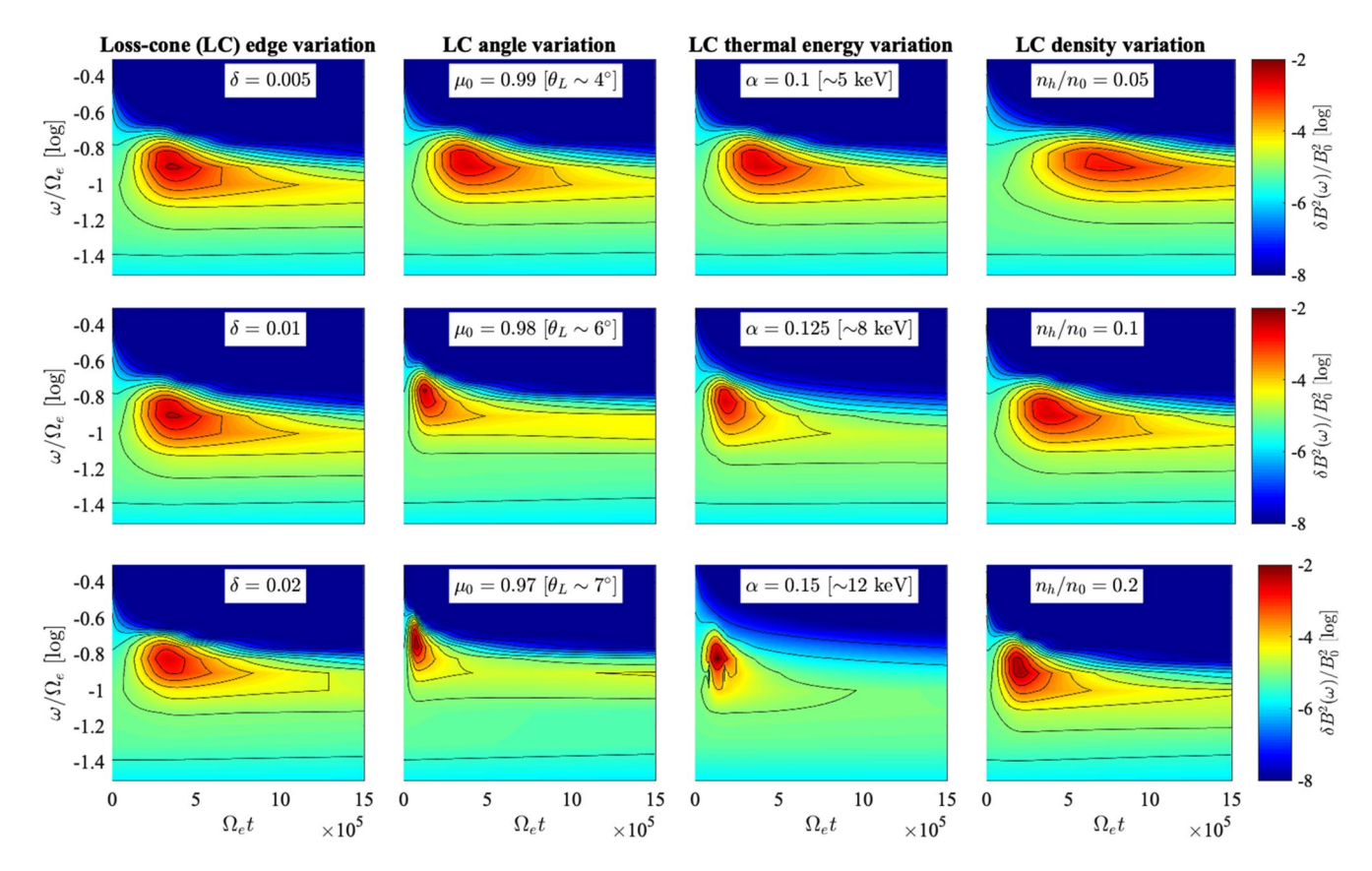


Figure 7. Dependence of the frequency-time spectrogram of the whistler mode chorus wave on some key parameters. The first panels from left show the variation on the loss-cone boundary sharpness parameter  $\delta$ . The second panels depict the variation of the loss-cone angle  $\theta_L$ . The third panels illustrate the sensitivity of the spectrum on thermal energy associated with the loss-cone electrons as parametrized by  $\alpha$ . The right most panels depict the dependence on the loss-cone electron density normalized to the net density  $n_h/n_0$ . Of these, the result is most insensitive to  $\delta$ . The loss-cone angle of more than a few degrees is probably not applicable for low-latitude observations. Thermal energy of  $\sim$ 5 keV is also consistent with JADE observation. Hence, other cases are considered as an academic exercise. The density ratio  $n_h/n_0$  is unknown although it is expected to be low. We considered three cases  $n_h/n_0 = 0.005$ , 0.1, and 0.2.

times and locations, but we cannot know precisely which effects are temporal or spatial, as both are changing during the observations. We also have some evidence that a plasma injection occurred during this period because of a modest increase in the large scale particle flux at multiple times (and locations) during the observations, which means that the spacecraft observation may comprise wave emissions from multiple sources. According to theory the whistler mode chorus emissions must be characterized by quasi-oblique angles of propagation. Gathering all these pieces of information, we illustrate the situation in Figure 8, where the local magnetic field lines, multiple sources of loss-cone electrons possessing slightly different input conditions, quasi-perpendicular whistler mode

waves, and the satellite trajectory are depicted. The observed chorus emission could be the result of cumulative sources.

Loss-cone electron phase-space distributions

Whistler mode spectra

Figure 8. A cartoon representation of Juno whistler chorus observation.

To further illustrate by a slightly more quantitative means, we have superposed all the cases considered in Figure 7 by artificially shifting the horizontal time axis for each case. We have then superposed all the spectra starting from left, the case with  $\mu_0 = 0.97$ , then for  $\mu_0 = 0.98$ , which is plotted with a shifted time axis, followed by  $\mu_0 = 0.99$ . Then we repeated with the case of  $\alpha = 0.15$ , 0.125, and 0.1, and with the spectra for  $\delta = 0.005$ , 0.01, and 0.02,  $n_{\rm h}/n_0 = 0.2$ ,  $n_{\rm h}/n_0 = 0.1$ , and finally, for  $n_{\rm h}/n_0 = 0.05$ . Each case is plotted with evenly shifted time axis. Of course, the ordering is totally arbitrary, and the interval for shifted time axis is also arbitrary, but the point we wish to emphasize is that the observed whistler chorus emission spectrum could be the result of cumulative sources all contributing to Juno observations. In order

YOON ET AL. 13 of 17

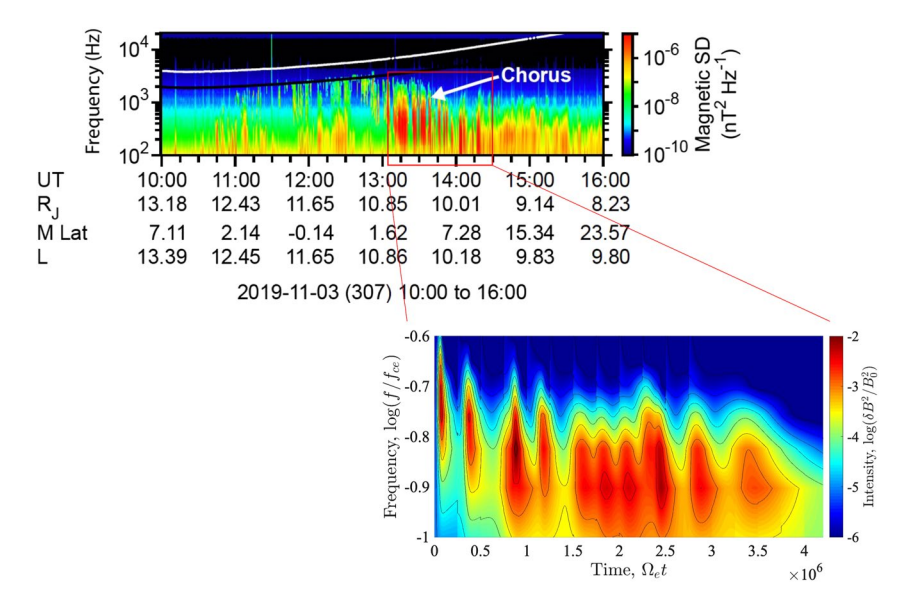


**Figure 9.** An artificial model of Juno whistler chorus emission (inset) constructed by superposing all the wave spectra considered in Figure 7, which is shown next to the actual observation.

to emphasize even further, we have placed the model cumulative wave spectrum next to the actual observation. The result is Figure 9.

### 5. Conclusions

In conclusion, the article successfully employed the reduced quasilinear theory that involves modeling the self-similar time dependent loss-cone electron distribution and solving for the time evolution of the underlying parameters that dictate the mathematical form of the model distribution. The time evolution of the most important parameter,  $\Delta$ , which determines the degree of loss-cone filling, is related to the velocity moment of the distribution. Consequently, the quasilinear theory amounts to calculating the evolution of velocity moments of the distribution, together with the instantaneous growth rate and evaluation of the wave kinetic equation. Of course, for actual situations, one cannot treat the entire problem with only temporal variation. As the spacecraft measurement is made in spatially varying medium one must, in principle, consider the spatio-temporal variation of underlying parameters, which is beyond the scope of the present work. Nevertheless, the present analysis shows that the basic methodology can be further extended to include spatial inhomogeneity effects. Among the anticipated effects due to spatial inhomogeneity is the fact that the electrons filling the loss cone via quasilinear saturation will eventually precipitate into the polar region of Jupiter. This effect is expected to lead to the replenishment of loss-cone feature at low latitude regions, which may further enhance the whistler mode excitation. To properly encapsulate such an effect requires a sophisticated analysis that includes treating the field-aligned variation of magnetic field and plasma density, coupled with appropriate boundary conditions.

We have taken appropriate physical input parameters that are relevant to the 3 November 2019 Juno observations, which is detailed in the article by Menietti et al. (2020). We found that the agreement with the observation is quite satisfactory in that the theoretically reconstructed frequency-time spectrogram of the whistler mode chorus emission—see Figure 6—compares rather well with observations. Specifically, it is found that the overall time scale of the whistler mode emission is on the order of an hour or so when translated to actual time, which is in qualitative agreement with observations—see Figure 4c. However, Juno traversed a region of chorus growth, and it is difficult to distinguish between spatial and temporal effects with a single satellite, as demonstrated in Figures 8 and 9 by quasi-Love wave analysis.

In Figure 4, it is seen that there exists a mild increase in the maximum electron energy, suggesting that Juno may be intercepting a region of recently injected high energy hot plasma as suggested by Menietti et al. (2020). More detailed discussions on the energetic electrons can be found in the article by Menietti et al. (2020), but in the present analysis, we do not consider any source (or sink) of energetic electrons. Instead, we regarded the entire

YOON ET AL. 14 of 17



whistler mode chorus emission as an initial value problem. In the future, however, we may entertain the problem from the perspective of a finite source or sink in both particles and waves, thereby making the analysis more relevant to actual observation. Furthermore, we may also include the effects of spatial inhomogeneity associated with the magnetic field as well as the ambient density. In any event, in view of the present assumption of initial value problem, we did not find much change in the electron thermal energy. However, the excited whistler waves may lead to an acceleration of a small population of seed energetic electrons to much higher energies, but this process is not included in the present discussion.

To recap the present article, we found that the present quasilinear velocity moment approach can be an efficient yet reliable research tool to analyze the wave emissions in the Jovian magnetospheric environment. This type of analysis can obviously be extended to other wave modes and radiations, such as kilometric, hectometric, and decametric radiations (Louarn et al., 2017; Louis et al., 2019). In order to extend the present analysis to include other wave modes one must first generalize the whistler mode dispersion relation (Equation 4) to include other modes. The whistler mode dispersion relation (Equation 4) is a reduced version of the so-called W mode among the so-called magneto-ionic theory of cold-plasma waves, which includes the fast extraordinary (X) and ordinary (X) modes, and the slow extraordinary (X) mode, of which the upper-hybrid mode is part of. The kilometric, hectometric, and decametric radiations operate on X (and/or X0) mode(s). While the upper-hybrid or X1 mode instability maybe treated in the same non-relativistic quasilinear theory as in this article, the radiations require the inclusion of relativistic cyclotron resonance condition. These generalization and extensions further complicate the analysis, but they can be done. Needless to say, however, such tasks are the subject of future studies.

### **Data Availability Statement**

Juno Waves data used in the generation of the figures of this work are located at NASA Planetary Data System website, https://pds-ppi.igpp.ucla.edu/data/JNO-E\_J\_SS-WAV-3-CDR-SRVFULL-V1.0. JADE calibrated data are located at https://pds-ppi.igpp.ucla.edu/data/JNO-J\_SW-JAD-3-CALIBRATED-V1.0/. The MAG calibrated data are located at https://pds-ppi.igpp.ucla.edu/data/JNO-SS-3-FGM-CAL-V1.0/ and at https://pds-ppi.igpp.ucla.edu/data/JNO-J-3-FGM-CAL-V1.0. The data used to generate Figure 3 of this article can be found in tabular form at https://doi.org/10.5281/zenodo.5663916. The theoretical plots are in normalized units, and the equations are clearly explained in the text. Therefore, no actual data are generated by the theory.

### ${\bf Acknowledgments}$

P. H. Yoon acknowledges NASA Grant NNH18ZDA001N-HSR and NSF Grant 1842643 to the University of Maryland. P. H. Yoon acknowledges fruitful discussions with Lunjin Chen. J. D. Menietti acknowledges support from NASA grant 80NSSC19K1262. Research conducted at the University of Iowa (W. S. Kurth) was supported by NASA New Frontiers Program through Contract 699041X with Southwest Research Institute. F. Allegrini and S. J. Bolton were funded by NASA New Frontiers Program for Juno.

### References

- Allegrini, F., Bagenal, F., Bolton, S., Connerney, J., Clark, G., Ebert, R. W., et al. (2017). Electron beams and loss cones in the auroral regions of Jupiter. *Geophysical Research Letters*, 44, 7131–7139. https://doi.org/10.1002/2017GL073180
- Allegrini, F., Mauk, B., Clark, G., Gladstone, G. R., Hue, V., Kurth, W. S., et al. (2020). Energy flux and characteristic energy of electrons over Jupiter's main auroral emission. *Journal of Geophysical Research: Space Physics*, 125, e2019JA027693. https://doi.org/10.1029/2019JA027693

  Allison, H. J., & Shprits, Y. Y. (2020). Local heating of radiation belt electrons to ultra-relativistic energies. *Nature Communications*, 11, 4533. https://doi.org/10.1038/s41467-020-18053-z
- Baker, D. N., Kanekal, S. G., Hoxie, V. C., Henderson, M. G., Li, X., Spence, H. E., et al. (2013). A long-lived relativistic electron storage ring embedded in Earth's outer Van Allen belt. Science, 340, 186–190. https://doi.org/10.1126/science.1233518
- Bolton, S. J., Thorne, R. M., Gurnett, D. A., Kurth, W. S., & Williams, D. J. (1997). Enhanced whistler-mode emissions: Signatures of interchange motion in the Ion torus. *Geophysical Research Letters*, 24, 2123–2126. https://doi.org/10.1029/97gl02020
- Bortnik, J., Thorne, R. M., & Meredith, N. P. (2008). The unexpected origin of plasmaspheric hiss from discrete chorus emissions. *Nature*, 452(7183), 62–66. https://doi.org/10.1038/nature06741
- Bortnik, J., Thorne, R. M., Meredith, N. P., & Santolík, O. (2007). Ray tracing of penetrating chorus and its implications for the radiation belts. Geophysical Research Letters, 34, L15109. https://doi.org/10.1029/2007GL030040
- Boyd, A. J., Turner, D. L., Reeves, G. D., Spence, H. E., Baker, D. N., & Blake, J. B. (2018). What causes radiation belt enhancements: A survey of the Van Allen Probes era. *Geophysical Research Letters*, 45, 5253–5259. https://doi.org/10.1029/2018GL077699
- Chen, Y., Reeves, G. D., & Freidel, R. H. W. (2007). The energization of relativistic electrons in the outer Van Allen radiation belt. *Nature Physics*, 3, 614–617. https://doi.org/10.1038/nphys655
- Cowley, S. W. H., & Bunce, E. J. (2003). Modulation of Jovian middle magnetosphere currents and auroral precipitation by solar wind-induced compressions and expansions of the magnetosphere: Initial response and steady state. *Planetary and Space Science*, 51, 31–56. https://doi.org/10.1016/s0032-0633(02)00130-7
- Elliott, S. S., Gurnett, D. A., Kurth, W. S., Mauk, B. H., Ebert, R. W., Clark, G., et al. (2018). The acceleration of electrons to high energies over the Jovian polar cap via whistler mode wave-particle interactions. *Journal of Geophysical Research: Space Physics*, 123, 7523–7533. https://doi.org/10.1029/2018JA025797
- Elliott, S. S., Gurnett, D. A., Yoon, P. H., Kurth, W. S., Mauk, B. H., Ebert, R. W., et al. (2020). The generation of upward-propagating whistler mode waves by electron beams in the Jovian polar regions. *Journal of Geophysical Research: Space Physics*, 125, e2020JA027868. https://doi.org/10.1029/2020JA027868

YOON ET AL. 15 of 17



- Eyelade, A. V., Stepanova, M., Espinoza, C. M., & Moya, P. S. (2021). On the relation between Kappa distribution functions and the plasma beta parameter in the Earth's magnetosphere: THEMIS observations. *Astrophysical Journal Supplement Series*, 253, 34. https://doi.org/10.3847/1538-4365/abdec9
- Gao, X., Mourenas, D., Li, W., Artemyev, A. V., Lu, Q., Tao, X., & Wang, S. (2016). Observational evidence of generation mechanisms for very oblique lower band chorus using THEMIS waveform data. *Journal of Geophysical Research: Space Physics*, 121, 6732–6748. https://doi.org/10.1002/2016JA022915
- Horne, R. B., Throne, R. M., Glauert, S. A., Menietti, J. D., Shprits, Y. Y., & Gurnett, D. A. (2008). Gyro-resonant electron acceleration at Jupiter. Nature Physics, 4, 301–304. https://doi.org/10.1038/nphys897
- Imai, M., Kurth, W. S., Hospodarsky, G. B., Bolton, S. J., Connerney, J. E. P., & Levin, S. M. (2017c). Direction-finding measurements of Jovian low-frequency radio components by Juno near Perijove 1. Geophysical Research Letters, 44, 6508–6516. https://doi.org/10.1002/2017GL072850
- Imai, M., Kurth, W. S., Hospodarsky, G. B., Bolton, S. J., Connerney, J. E. P., & Levin, S. M. (2017b). Statistical study of latitudinal beaming of Jupiter's decametric radio emissions using Juno. Geophysical Research Letters, 44, 4584–4590. https://doi.org/10.1002/2017GL073148
- Imai, M., Kurth, W. S., Hospodarsky, G. B., Bolton, S. J., Connerney, J. E. P., Levin, S. M., et al. (2017a). Latitudinal beaming of Jovian decametric radio emissions as viewed from Juno and the Nançay Decameter Array. Geophysical Research Letters, 44, 4455–4462. https://doi.org/10.1002/2016GL072454
- Katoh, Y., Tsuchiya, F., Miyoshi, Y., Morioka, A., Misawa, H., Ujiie, R., et al. (2011). Whistler mode chorus enhancements in association with energetic electron signatures in the Jovian magnetosphere. *Journal of Geophysical Research: Space Physics*, 116. https://doi.org/10.1029/2010JA016183
- Kurth, W. S., Hospodarsky, G. B., Kirchner, D. L., Mokrzycki, B. T., Averkamp, T. F., Robison, W. T., et al. (2017). The Juno waves investigation. Space Science Reviews, 213, 347–392. https://doi.org/10.1007/s11214-017-0396-y
- Kurth, W. S., Mauk, B. H., Elliott, S. S., Gurnett, D. A., Hospodarsky, G. B., Santolik, O., et al. (2018). Whistler mode waves associated with broadband auroral electron precipitation at Jupiter. Geophysical Research Letters, 45, 9372–9379. https://doi.org/10.1029/2018GL078566
- Lee, S.-Y., Lee, E., Seough, J., Lee, J.-J., Hwang, J., Lee, J.-J., et al. (2018). Simulation and quasilinear theory of whistler anisotropy instability. Journal of Geophysical Research: Space Physics, 123, 3227–3290. https://doi.org/10.1029/2017JA024960
- Lee, J., Yoon, P. H., Seough, J., Hwang, J., Lee, J., Choe, G., & Choe, G. S. (2018). Simulation and quasilinear theory of magnetospheric Bernstein mode instability. *Journal of Geophysical Research: Space Physics*, 123, 7320–7331. https://doi.org/10.1029/2018JA025667
- stein mode instability. *Journal of Geophysical Research: Space Physics*, 123, 7320–7331. https://doi.org/10.1029/2018JA025667
  Li, W., Shen, X.-C., Menietti, J. D., Ma, Q., Zhang, X.-J., Kurth, W. S., & Hospodarsky, G. B. (2020). Global distribution of whistler mode waves
- in Jovian inner magnetosphere. Geophysical Research Letters, 46, e2020GL088198. https://doi.org/10.1029/2020GL088198
  Louarn, P., Allegrini, F., McComas, D. J., Valek, P. W., Kurth, W. S., André, N., et al. (2017). Generation of the Jovian hectometric radiation: First
- lessons from Juno. Geophysical Research Letters, 44, 4439–4446. https://doi.org/10.1002/2017GL072923

  Louarn, P., Paranicas, C. P., & Kurth, W. S. (2014). Global magnetodisk disturbances and energetic particle injections at Jupiter. Journal of Geo-
- physical Research: Space Physics, 119, 4495–4511. https://doi.org/10.1002/2014JA019846
  Louis, C. K., Prangé, R., Lamy, L., Zarka, P., Imai, M., Kurth, W. S., & Connerney, J. E. P. (2019). Jovian auroral radio sources detected in situ
- by Juno/waves: Comparisons with model auroral ovals and simultaneous HST FUV images. *Geophysical Research Letters*, 46(11), 606614–611614. https://doi.org/10.1029/2019GL084799

  Mauk, B. H., Haggerty, D. K., Paranicas, C., Clark, G., Kollmann, P., Rymer, A. M., et al. (2018). Diverse electron and ion acceleration character-
- istics observed over Jupiter's main aurora. Geophysical Research Letters, 45, 1277–1285. https://doi.org/10.1002/2017GL076901

  McComas, D. J. Alexander, N. Allegrini, F. Bagenal, F. Beebe, C. Clark, G. et al. (2017). The Joyian Auroral Distributions Experiment
- McComas, D. J., Alexander, N., Allegrini, F., Bagenal, F., Beebe, C., Clark, G., et al. (2017). The Jovian Auroral Distributions Experiment (JADE) on the Juno mission to Jupiter. *Space Science Reviews*, 213, 547–643. https://doi.org/10.1007/s11214-013-9990-9
- Melrose, D. B. (1986). Instabilities in space and laboratory plasmas. Cambridge University Press.
- Menietti, J. D., Averkamp, T. F., Imai, M., Kurth, W. S., Clark, G. B., Allegrini, F., et al. (2020). Low-latitude whistler-mode and higher-latitude Z-mode emission at Jupiter observed by Juno. *Journal of Geophysical Research: Space Physics*, 126, e2020JA028742. https://doi.org/10.1029/2020JA028742
- Menietti, J. D., Palmaerts, B., Zahlava, J., Averkamp, T. F., Groene, J. B., & Kurth, W. S. (2019). Quasiperiodic Saturn auroral hiss observed during a Cassini proximal orbit. *Journal of Geophysical Research: Space Physics*, 125, e2019JA027338. https://doi.org/10.1029/2019JA027338
- Menietti, J. D., Yoon, P. H., Pisa, D., Averkamp, T. F., Sulaiman, A. H., Kurth, W. S., et al. (2019). The role of intense upper hybrid resonance emissions in the generation of Saturn narrowband emission. *Journal of Geophysical Research: Space Physics*, 124, 5709–5718. https://doi. org/10.1029/2019JA026855
- Menietti, J. D., Yoon, P. H., Písa, D., Ye, S.-Y., Santolik, O., Arridge, C. S., et al. (2016). Source region and growth analysis of narrowband Z-mode emission at Saturn: Saturn Z-mode source region & growthrate. *Journal of Geophysical Research: Space Physics*, 121(12), 11929–111942. https://doi.org/10.1002/2016JA022913
- Reeves, G. D., Spence, H. E., Henderson, M. G., Morley, S. K., Friedel, R. H. W., Funsten, H. O., et al. (2013). Electron acceleration in the heart of the Van Allen radiation belts. *Science*, 341, 991–994. https://doi.org/10.1126/science.1237743
- Santolík, O., Chum, J., Parrot, M., Gurnett, D. A., Pickett, J. S., & Cornilleau-Wehrlin, N. (2006). Propagation of whistler mode chorus to low altitudes: Spacecraft observations of structured ELF hiss. *Journal of Geophysical Research: Space Physics*, 111, A10208. https://doi. org/10.1029/2005JA011462
- Seough, J., Yoon, P. H., & Hwang, J. (2014). Quasilinear theory and PIC simulation of proton cyclotron instability. *Physics of Plasmas*, 21, 062118. https://doi.org/10.1063/1.4885359
- Seough, J., Yoon, P. H., & Hwang, J. (2015). Simulation and quasilinear theory of proton firehose instability. *Physics of Plasmas*, 22, 012303. https://doi.org/10.1063/1.4905230
- Shprits, Y. Y., Kellerman, A. C., Drozdov, A. Y., Spence, H. E., Reeves, G. D., & Baker, D. N. (2015). Combined convective and diffusive simulations: VERB-4D comparison with 17 March 2013 Van Allen Probes observations. Geophysical Research Letters, 42, 9600–9608. https://doi.org/10.1002/2015GL065230
- Shprits, Y. Y., Menietti, J. D., Gu, X., Kim, K. C., & Horne, R. B. (2012). Gyroresonant interactions between the radiation belt electrons and whistler mode chorus waves in the radiation environment of Earth, Jupiter, and Saturn: A comparative study. *Journal of Geophysical Research: Space Physics*, 117(A11). https://doi.org/10.1029/2012JA018031
- Sibeck, D. G., McEntire, R. W., Lui, A. T. Y., Lopez, R. E., & Krimigis, S. M. (1987). Magnetic field drift shell splitting: Cause of unusual dayside particle pitch angle distributions during storms and substorms. *Journal of Geophysical Research: Space Physics*, 92, 13485–13497. https://doi.org/10.1029/ja092ia12p13485
- Stix, T. H. (1992). Waves in plasmas. Springer-Verlag.
- Tigik, S. F., Ziebell, L. F., Yoon, P. H., & Kontar, E. P. (2016). Two-dimensional time evolution of beam-plasma instability in the presence of binary collisions. Astronomy & Astrophysics, 586, A19. https://doi.org/10.1051/0004-6361/201527271

YOON ET AL. 16 of 17



- Tyler, E., Breneman, A., Cattell, C., Wygant, J., Thaller, S., & Malaspina, D. (2019). Statistical occurrence and distribution of high-amplitude whistler mode waves in the outer radiation belt. *Geophysical Research Letters*, 46, 2328–2336. https://doi.org/10.1029/2019GL082292
- Woodfield, E. E., Horne, R. B., Glauert, S. A., Menietti, J. D., & Shprits, Y. Y. (2014). The origin of Jupiter's outer radiation belt. *Journal of Geophysical Research: Space Physics*, 119, 3490–3502. https://doi.org/10.1002/2014JA019891
- Xiong, Y., Chen, L., Xie, L., Fu, S., Xia, Z., & Pu, Z. (2017). Relativistic electron's butterfly pitch angle distribution modulated by localized background magnetic field perturbation driven by hot ring current ions. *Geophysical Research Letters*, 44, 4393–4400. https://doi.org/10.1002/2017GL072558
- Yates, J. N., Southwood, D. J., Dougherty, M. K., Sulaiman, A. H., Masters, A., Cowley, S. W. H., et al. (2016). Saturns's quasi-periodic magnetohydrodynamic waves: Saturn's quasi-periodic MHD waves. *Geophysical Research Letters*, 43(21), 102–111. https://doi.org/10.1002/2016g1071069
- Yoon, P. H., Lee, J., Seough, J., Hwang, J., & Choe, G. S. (2019). Whistler instability driven by electron thermal ring distribution with magneto-spheric application. *Journal of Geophysical Research: Space Physics*, 124, 5289–5301. https://doi.org/10.1029/2019JA026687
- Yoon, P. H., Weatherwax, A. T., & Rosenberg, T. J. (1998). On the generation of auroral radio emissions at harmonics of the lower ionospheric electron cyclotron frequency: X, O, and Z mode maser calculations. *Journal of Geophysical Research: Space Physics*, 103, 4071–4078. https://doi.org/10.1029/97ja03526

YOON ET AL. 17 of 17